A Density Functional Theory Study of the Ionic and Electronic Transport Mechanisms in $LiFeBO_3$ Battery Electrodes

Loftager, Simon; García Lastra, Juan Maria; Vegge, Tejs

Published in:
Journal of Physical Chemistry C

Link to article, DOI:
10.1021/acs.jpcc.6b03456

Publication date:
2016

Document Version
Peer reviewed version

A Density Functional Theory Study of the Ionic and Electronic Transport Mechanisms in $LiFeBO_3$ Battery Electrodes

Simon Loftager, Juan María García-Lastra, Tejs Vegge*

Department of Energy Conversion and Storage, Technical University of Denmark, Fysikvej, 2800 Kgs. Lyngby, Denmark

ABSTRACT: Lithium iron borate is an attractive cathode material for Li-ion batteries, due to its high specific capacity and low-cost, earth-abundant constituents. However, experiments have observed poor electrochemical performance due to the formation of an intermediate phase, i.e., Li_xFeBO_3, which leads to large overvoltages at the beginning of charge. Using a convex-hull analysis, based on Hubbard-corrected density functional theory (DFT+*U*), we identify this intermediate phase as $Li_{0.5}FeBO_3$. Moreover, we show by means of the nudged elastic band (NEB) method, that the origin of these adverse electrochemical effects can be explained by an intrinsically low Li-ion and electron/hole-polaron mobility in $Li_{0.5}FeBO_3$ due to high activation barriers for both the ionic and electronic transport. These studies include the effects of the experimentally reported commensurate modulation. We have also investigated the Li-ion/hole diffusion through the interface between $Li_{0.5}FeBO_3$ and $LiFeBO_3$, which is found not to result in additional kinetic limitations from Li diffusion across the intraparticle interfaces. These findings suggest that the experimentally observed diminished performance associated with the formation of intermediate phases is linked to the intrinsically poor properties of the $Li_{0.5}FeBO_3$ phase rather than to the presence of interfaces between different phases.

1. INTRODUCTION

Lithium-ion batteries (LIBs) are now the dominating energy-storage medium for portable electronic devices and may provide an important step towards the improvement of storage of sustainable energy from intermittent sources such as wind, solar and hydroelectric power, in the form of large-scale battery grids enabling load leveling and peak shaving. In addition, LIBs provide the backbone for the growing demand for transportable energy storage in electric vehicles (EVs).

The heaviest electroactive component of a battery is the cathode and thus much research has focused on improving upon its energy density and power density. Among the most popular cathode materials is the layered transition-metal oxide, $LiNi_{1/3}Mn_{1/3}Co_{1/3}O_2$ (NMC), which combines a high theoretical capacity of 278 mAh/g and excellent cyclability,[1] but is limited by the toxicity and high cost of Co. A promising alternative to the layered transition-metal oxides is the transition-metal olivine-structured materials, such as $LiFePO_4$, which consists of earth-abundant, environmentally benign elements. However, $LiFePO_4$ suffers from a low rate capability resulting from low ionic and electronic conductivity, which can only be alleviated by down-sizing the particles of the active material, decreasing the volumetric energy density of the cathode material. Another member of the polyanionic

structure class is lithium iron borate, $LiFeBO_3$, which enjoys a high theoretical specific capacity of 220 mAh/g and displays volume changes shown to be as small as 2 % compared to 6.7 % for the delithiation of $LiFePO_4$.[2] This significantly lowers the risk of the electrode material cracking during Li insertion and extraction, and thereby preventing loss of contact between the active cathode material and current collector, thereby resulting in an increase in the expected lifetime and overall battery performance. However, in many other applications of today's battery systems, an important requirement is fast charge and recharge properties. This puts severe restrictions on a number of available cathode materials, since both a low ionic and low electronic mobility will decrease the rate capability and achievable capacity of the cathode.[3] Since many of the limitations on the rate capability of the cathode materials are caused by issues related to the electronic and ionic transport in the bulk and across external interfaces (e.g., carbon coating on an electrode) and internal interfaces (e.g., the interface between regions with different Li concentrations), improvements on these properties require a detailed understanding of the reactions occurring at the interfaces at the atomic level. Such detailed insights can be accessed through advanced computational techniques, where, in particular, density functional theory (DFT)[4,5] offers a compelling compromise between accuracy and computational cost, for instance in studies involving fast screening of a wide range of materials properties as compared to conventional experimental techniques[6]. Not surprisingly, DFT studies have played a key role in determining the dominating transport mechanisms for Li ions (Li ions at Li-ion lattice sites in the cathode material) and holes (lattice sites where Li ions have been removed) in lithium transition-metal phosphates[7] and borates,[8] as well as for electrons and holes in lithium transition-metal phosphates[9] and Li–air batteries[10–12].

In general, the formation of interfaces during charge/discharge has a large impact on electrochemical properties, such as rate capability, achievable capacity and voltage. In the case of $LiFePO_4$, the (de)lithiation mechanism in $LiFePO_4$ has been suggested to proceed via a two-phase reaction between the endmembers, $Li_{0.97}FePO_4$ and $Li_{0.03}FePO_4$.[13] Since $LiFePO_4$ and $LiFeBO_3$ both have been shown to have their Li diffusion confined to channels[8,14] (along the *b*-axis in $LiFePO_4$ and along the *c*-axis in $LiFeBO_3$), a natural question is whether the two compounds share the same (de)intercalation mechanism, i.e., whether the (de)lithiation of $LiFeBO_3$ proceeds via a two-phase reaction. Galvanostatic intermittent titration technique (GITT) experiments on carbon-coated $LiFeBO_3$ nanoparticles performed by Yamada et al.[2] have revealed a continuous shift of diffraction peaks in the lattice parameters and a sloping OCV curve of Li_xFeBO_3, indicating a solid-solution-type behavior in the approximate Li-concentration range of $0.15 \leq x \leq 0.5$ (i.e., during the initial stage of discharge). Their GITT experiments and DFT studies suggested that in the Li-concentration range $0.5 \leq x \leq 1.0$ one or more two-phase reactions occurred, which was unambiguously corroborated by Bo et al.[15], who later reported indications of the existence of a stable interface between regions of $LiFeBO_3$ and $Li_{0.5}FeBO_3$ phases[16].

Here, we first present a thermodynamic stability analysis of the possible compounds between the compositions $FeBO_3$ and $LiFeBO_3$, which reveals a stable intermediate phase at half lithiation, i.e., at

$Li_{0.5}FeBO_3$. Secondly, the diffusion barriers of Li ions in $FeBO_3$ and Li holes in $LiFeBO_3$ and Li ions in the most stable configuration of $Li_{0.5}FeBO_3$ are calculated and a significant lowering of the diffusivity in $Li_{0.5}FeBO_3$—as compared to the diffusivities in $LiFeBO_3$/$FeBO_3$—is predicted to take place.

Internal interfaces which may form during the initial-stage delithiation are also investigated and the Li-defect diffusion across the interfaces themselves is determined not to lower the overall Li transport in $LiFeBO_3$. Seo et al.[8] calculated a 3.19 eV bandgap in $LiFeBO_3$, which is large enough to prevent the thermal activation of electrons or holes, and ascribed the electronic conduction to electron and hole polarons, i.e., states where the excess charge is carried by a local distortion of the lattice. We prove the existence of these electron and hole polarons localizing on Fe ions and furthermore, the hopping mechanisms of these polarons in relevant phases of bulk Li_xFeBO_3 are investigated and we show that the most stable Li configuration in $Li_{0.5}FeBO_3$ lowers the electronic mobility relative to both $LiFeBO_3$ and $FeBO_3$. These findings strongly suggest that the Li (de)intercalation in $LiFeBO_3$ is intrinsically impeded by the transport of Li ions and electron/hole polarons, in particular in the $Li_{0.5}FeBO_3$ phase.

2. METHODOLOGY

2.1 The crystal structure of $LiFeBO_3$. Early experimental reports[17] showed that lithium iron borate ($LiFeBO_3$) has a monoclinic crystal symmetry in which chains of edge-sharing FeO_5 trigonal bipyramids align along the [-101] direction, and chains of LiO_4 tetrahedra in pairs run along the [001] direction with planar BO_3 groups connecting the edge-sharing FeO_5 chains. The DFT-optimized geometry of this structure is shown in Figure 1. X-ray diffraction studies by Janssen et al.[18] revealed that a commensurately modulated superstructure exists in $LiFeBO_3$, which effectively doubles the unit cell along the *a*-axis and displaces the Li ions out of the trigonal bipyramidal equatorial planes towards the center of the four neighboring O ions and altering the crystal symmetry from C2/*c* to C2/*c*(α0γ)00. Following Janssen et al.[18], the modulation of $LiFeBO_3$ giving rise to the C2/*c*(α0γ)00 crystal symmetry was also here modeled in a $P2_1/c$ crystal symmetry, and the lattice parameters and atomic positions used as a starting point for our structure optimizations of the modulated $LiFeBO_3$ were those reported by Janssen et al.[18] (their Table S7): a = 10.3469 Å, b = 8.9209 Å, c = 10.2528 Å, β = 90.878 °. In order to assess the stability of the modulated (as modeled in the $P2_1/c$ symmetry) versus unmodulated (C2/*c* symmetry) $LiFeBO_3$, calculations on unmodulated $LiFeBO_3$ were started with the lattice parameters reported by Janssen et al.[18]: a = 5.1350 Å, b = 9.0437 Å, c = 10.2907 Å and β = 91.031 °. Upon Li extraction (charge) of $LiFeBO_3$ the oxidation occurs on the Fe^{2+} ions, which become Fe^{3+} ions. The Fe ions are always determined to be in their high-spin state having their five 3*d* orbitals occupied. Therefore, Fe in $LiFeBO_3$ is Fe^{2+} and Fe in $FeBO_3$ is Fe^{3+} possessing a magnetic moment of 4 μ_B and 5 μ_B, respectively.

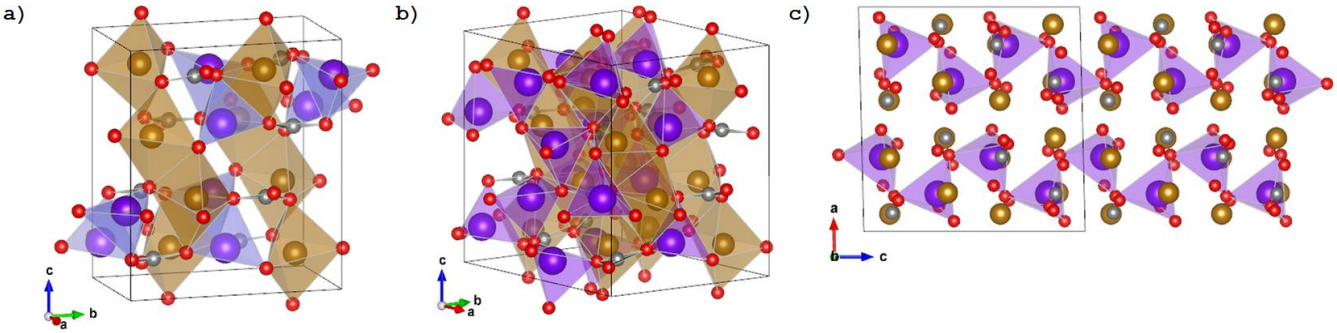

Figure 1. (a) Unit cell of the DFT-optimized unmodulated $LiFeBO_3$ structure showing Fe atoms in brown residing in brown FeO_5 complexes linked together to form chains running in the [-101] direction and Li atoms in purple residing in purple LiO_4 complexes running in the [001] direction. (b) Unit cell of DFT-optimized modulated $LiFeBO_3$ structure. (c) Corner-sharing LiO_4 complexes running in the [001] direction in modulated $LiFeBO_3$. Boron atoms are gray and oxygen atoms are red. (Images generated with the VESTA software package[19].)

2.2 Computational methods. In this study, all structures were set up and analyzed using the Atomic Simulation Environment (ASE) package[20] and relaxed to their ground state by solving the electronic-structure problem within density functional theory (DFT). The Vienna Ab-initio Simulation Package (VASP)[21] was used in which plane waves were expanded up to a kinetic-energy cutoff of 500 eV and the projector-augmented-wave (PAW) method[22] was employed to describe the atomic cores. In the PAW pseudopotentials, for Li, B and O the 1s electrons were treated as core electrons and for Fe the electrons up to 3p (including 3p) were treated as core electrons. The exchange–correlation effects were described within the generalized-gradient approximation (GGA) by the Perdew–Burke–Ernzerhof (PBE) functional[23]. For the determination of the partial occupancies, the tetrahedron method with Blöchl corrections[24] were used and the electronic levels were smeared by 0.05 eV.

The incomplete cancellation of the electron self-interaction in the GGA often leads to significant deviations from experimental results, in particular the band gap,[25,26] which are due to the propensity of the self-interaction towards delocalizing the electrons, in particular for systems exhibiting a strong localization of the d-orbital electrons, as is the case of $LiFeBO_3$. This problem has previously[2,8] been alleviated by employing the Hubbard-U correction[27] and following Seo et al.[8], a value of U = 4.3 eV was therefore applied on the 3d orbitals of Fe in Li_xFeBO_3.

Three kinds of simulation cells were used: For the structural relaxation of the unit cell of $LiFeBO_3$, the k-point sampling was performed using a Monkhorst–Pack[28] (MP) mesh of 4×2×2, for the (2a,b,c) supercells a MP mesh of 2×2×2 was used and for the (a,b,2c) supercells a 4×2×1 MP mesh was used. Structures were relaxed until all forces did not exceed 0.05 eV/Å using the FIRE minimization algorithm[29]. The self-consistent solution to the Kohn–Sham equation was performed with an accuracy of 0.1 meV.

In our model, an electron (hole) polaron was simulated by adding (removing) an electron (hole) to the $FeBO_3$ ($LiFeBO_3$) supercell having a compensating background charge in order to maintain charge neutrality. The symmetry of the system was broken by stretching (compressing) the Fe–O bonds for a particular Fe ion in the supercell, around which the electron (hole) is expected to be localized. This approach enabled charge localization and lowered the computation time of the structural relaxations.

In order to determine the activation barriers of the Li-ion/hole jumps and polaron hops, the nudged elastic band (NEB) method[30] as implemented in ASE was employed with a total number of seven images, where the initial particle trajectory was created by linearly interpolating between the initial and final image. The energies and forces were calculated by VASP, and the forces were let to relax to the same threshold value as for the structure relaxations (0.05 eV/Å).

3. RESULTS AND DISCUSSION

3.1 Optimized lattice of $LiFeBO_3$. Our DFT calculations on modulated LiFeBO3 yields the optimized lattice parameters a = 10.409 Å, b = 8.9953 Å, c = 10.324 Å and β = 91.39 °, and for unmodulated $LiFeBO_3$ the lattice parameters relaxed to a = 5.1683, b = 9.1086 Å, c = 10.3485 Å and β = 91.283 °. The DFT calculations also reveal that the modulated phase of $LiFeBO_3$ is more stable than the unmodulated phase by 11 meV/f.u., agreeing well with the stability energy reported by Janssen et al.[18] of 12 meV/f.u. Both sets of lattice parameters are in good agreement with experimental values[18] (vide supra). As Janssen et al.[18] report, we find that the length of the apical Li–O bond (along the c-axis) in the LiO_4 tetrahedra is longer than the other Li–O bonds by approximately 0.1 Å in modulated $LiFeBO_3$. Upon full delithiation yielding $FeBO_3$, the lattice parameters relaxed to a = 5.3078 Å, b = 8.9894 Å, c = 10.1876 Å and β = 89.399 ° resulting in a volume change from modulated $LiFeBO_3$ to $FeBO_3$ of 0.6 %.

3.2 Thermodynamics of bulk Li_xFeBO_3. Experimental and computational results by Yamada et al.[2] and Bo et al.[16] suggest the possible existence of partially lithiated phases. Using the convex-hull method,[26] the phase stability of Li_xFeBO_3 at different Li concentrations were analyzed. In this method, the relative energy per formula unit at a given Li concentration, x, is given by

$$E_{\mathrm{rel}} \equiv E_{\mathrm{Li}_x\mathrm{FeBO}_3} - x\,E_{\mathrm{LiFeBO}_3} - (1-x)E_{\mathrm{FeBO}_3}, \qquad (1)$$

where $E_{\mathrm{Li}_x\mathrm{FeBO}_3}$ is the total energy obtained from DFT calculations for the respective structure per formula unit. The convex hull is constructed by connecting the most stable phases of the compound while ensuring that the curvature of the resulting curve is always positive. If the relative energy at a specific Li concentration is higher than the energy of the line joining the lowest-energy configurations at the neighboring Li concentrations (i.e., the convex hull), the corresponding phase is unstable relative to a blend of the phases at the neighboring Li concentrations. This scenario would correspond to a two-phase reaction and would result in a plateau in the voltage profile. For the construction of the convex

hull of Li_xFeBO_3, all symmetry-inequivalent Li arrangements in the unit cell of unmodulated Li_xFeBO_3 were investigated: For x = {0, 1/8, 7/8, 1}, 1 combination exists, for x = {1/4, 3/8, 5/8, 3/4}, 7 combinations exist, and for x = 1/2, 14 combinations exist. These structures were then doubled in the *a*-direction—so as to resemble the size of the unit cell of modulated $LiFeBO_3$—and fully relaxed. Naturally, the energy of the *a*-doubled unmodulated structures was twice the energy of the unit cell. The relative energies are shown in Figure 2(a) as black circles. Also, the Li configurations found in the unmodulated Li_xFeBO_3 structures were calculated with the modulation included, and these are shown in Figure 2(a) as black plusses. In order to extend the phase-stability model to include possible clustering of Li ions and holes, supercells were created by repeating the unit cell of unmodulated Li_xFeBO_3 in the *a*-direction. The selected Li configurations in these supercells were determined as those minimizing or maximizing the Coulomb repulsion between the Li ions, yielding an additional 14 structures (i.e., two different structures for the seven intermediate configurations). The relative energies obtained from the supercell configurations of unmodulated Li_xFeBO_3 are included as red circles. Additionally, the Li configurations found in unmodulated Li_xFeBO_3 structures maximizing/minimizing the Coulomb repulsion were calculated with the modulation included, and these are shown in Figure 2(a) as red plusses. Figure 2(b) shows the profile for the open-circuit voltage (OCV) calculated by

$$U_{\mathrm{OCV}}(x) = -\frac{E_{\mathrm{Li}_{x_2}\mathrm{FeBO}_3} - E_{\mathrm{Li}_{x_1}\mathrm{FeBO}_3} - (x_2 - x_1)E_{\mathrm{Li(s)}}}{(x_2 - x_1)e}, \quad x_1 < x < x_2, \quad (2)$$

where the energies, E, are calculated using DFT and $E_{\mathrm{Li(s)}}$ indicates that all voltages are calculated with respect to the Li-metal electrode.

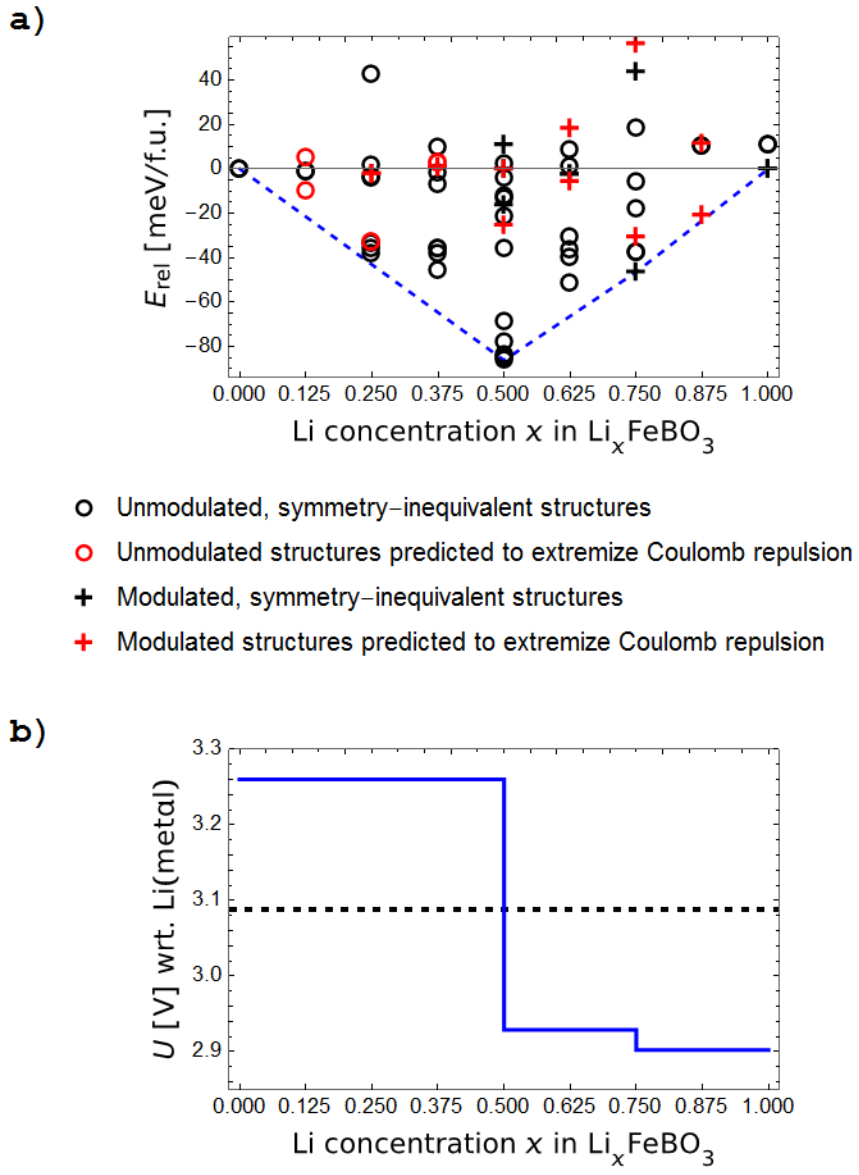

Figure 2. (a) The convex-hull construction showing relative energies for all possible Li configurations in a unit cell of Li_xFeBO_3, calculated in a *a*-doubled cell, indicated by black markers (circle: unmodulated structure; cross: modulated structure), and *a*-doubled structures minimizing or maximizing the Coulomb repulsion, indicated by red markers, calculated by Equation 1. The convex hull is indicated by the blue dashed line. (b) The voltage profile calculated by Equation 2 using the convex-hull energies in (a) is shown as a blue line and the equilibrium potential, $U_{\mathrm{eq}} = \frac{E_{\mathrm{LiFeBO_3}} - \left(E_{\mathrm{FeBO_3}} + 16E_{\mathrm{Li(s)}}\right)}{16e}$, is shown as a black dashed line.

The convex-hull construction in Figure 2(a) shows that the lowest-energy Li configuration for the phases having Li concentration of x = 0.0, 0.25, 0.375, 0.5 and 0.625 is obtained from an *a*-doubled unit-cell structure. In the case of x = 0.125, the lowest-energy Li configuration is obtained from an

unmodulated unit-cell structure doubled in the *a*-direction, whereas for $x = 0.875$, the lowest-energy Li configuration is obtained from a modulated structure, though in both cases the Li ions are distributed such that the Coulomb repulsion between the Li ions is minimized. At the latter concentration, the modulated symmetry-inequivalent structure relaxes to that of the unmodulated one. It is also noteworthy, that it is primarily for Li concentrations of $x > 0.5$ where the modulated structure is more stable than the unmodulated structure having the same Li distribution. This tallies well with the suggestion of Bo et al.[16], that the modulation is lost in the delithiated phase and in other Li-deficient phases. The half-lithiated phase, $Li_{0.5}FeBO_3$, has the highest stability relative to the other calculated phases. The $Li_{0.75}FeBO_3$ phase predicted to be stable by Yamada et al.[2] is also predicted to be stable in our model, whereas the phase at $Li_{0.875}FeBO_3$ is not. This is reflected in the voltage profile in Figure 2(b), where three plateaus are seen, one at 3.26 V for $0.0 < x < 0.5$, one at 2.93 V for $0.5 < x < 0.75$ and one at 2.90 V for $0.75 < x < 1.0$ together with an equilibrium voltage of 3.08 V (dashed line), which compares well with experimental values of about 3.0 V.[2] The bending of the convex hull due to the stable phase at $x = 0.75$ results in a plateau splitting of 0.05 V between the voltage plateaus at $0.5 < x < 0.75$ and $0.75 < x < 1.0$, a voltage difference which is likely to be detectable only in very slow GITT experiments.

The crystal structure of the lowest-energy configuration in the half-lithiated phase is shown in Figure 3 and the positions of the Li ions in the lowest-energy Li configuration are given in Table S1 in Supporting Information. In this configuration, the unmodulated phase is favored above the modulated phase. It is seen that the lowest-energy configuration of $Li_{0.5}FeBO_3$ favors a pair-wise arrangement in which Li ions reside relatively close to each other (3.4 Å) in pairs with the *z* component of the center-of-mass position of these pairs alternating along the *b*-direction. Intuitively, one would expect the Fe^{2+} ions to be closest to the Li^+ ions, thereby minimizing the Coulomb repulsion between the Fe ions and the Li ions. This is indeed the case for the extreme phases, i.e., $LiFeBO_3$ containing one Li hole and $FeBO_3$ containing one Li ion. Interestingly, this is not the case for the most stable Li configuration of the half-lithiated phase, as the actual Fe^{2+}/Fe^{3+}-ion distribution in this phase is 61 meV/f.u. more stable than the Fe^{2+}/Fe^{3+}-ion distribution predicted to be the most stable by a model minimizing the Coulombic repulsion created by the Li^+ ions at the Fe sites. This suggests that the elastic relaxations of the lattice after adding or removing Li^+ ions and the Fe–Fe-ion interactions (electrostatic and magnetic) could play an important role in the stabilization of particular Fe^{2+}/Fe^{3+}-ion arrangements. The same analysis applied to the second, third and fourth most stable configuration of the $Li_{0.5}FeBO_3$ phase shows that the most favorable Fe^{2+}/Fe^{3+}-ion distribution is the one predicted by only including the effects of the Coulombic potential created by the Li^+ ions at the Fe sites. The more complex Fe^{2+}/Fe^{3+}-ion ordering in the lowest-energy half-lithiated phase is expected to yield a more complex energy landscape of Li-ion diffusion as compared to the active endmembers, in particular at low C rates, where the equilibrium structure is expected to form. However, for real materials synthesized at room temperature, entropic and kinetic effects result in the actual structure containing several of the lowest-

energy configurations. Nevertheless, the transport properties of this phase are expected to be representative for the defect configuration.

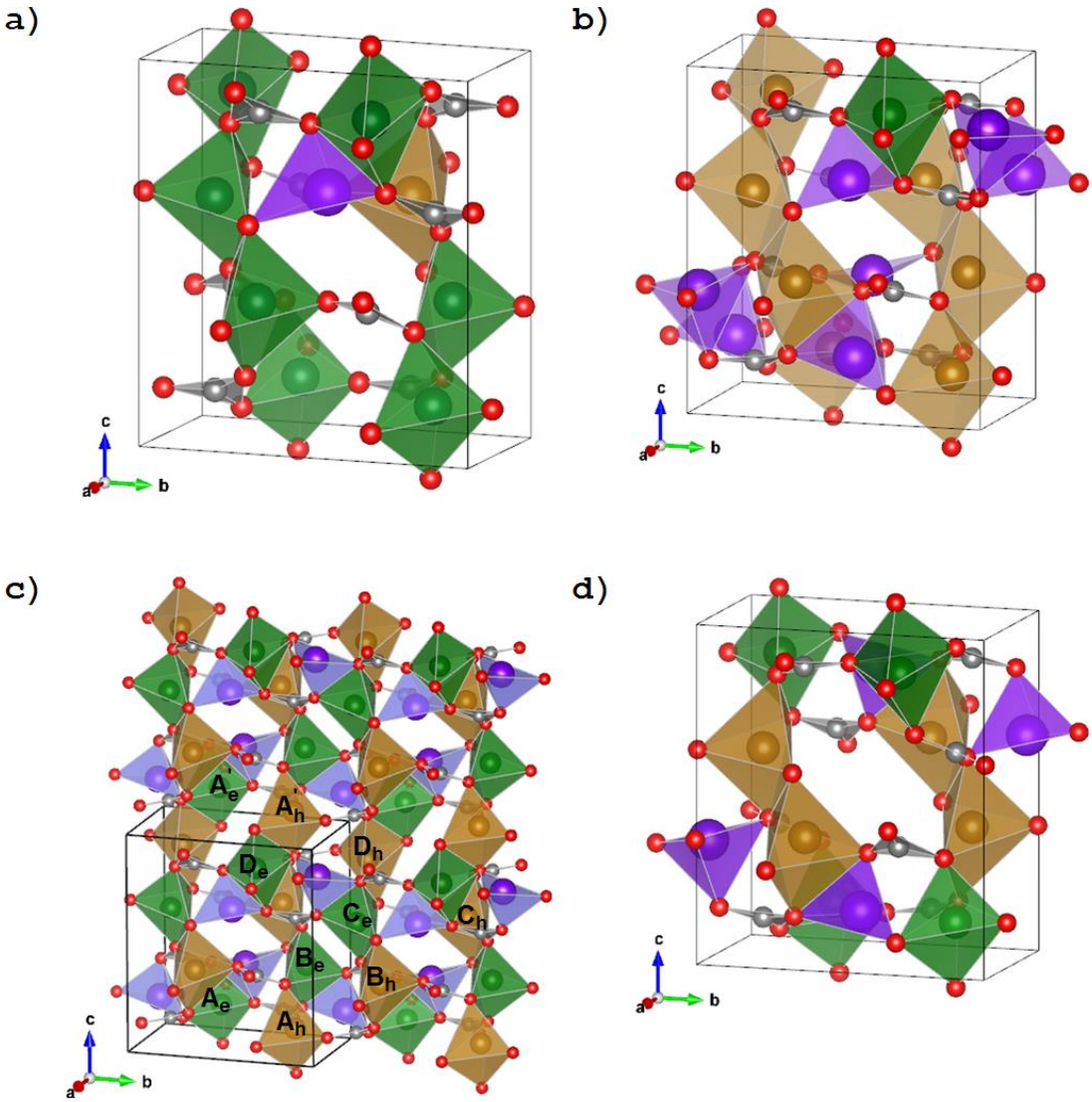

Figure 3. (a) $FeBO_3$ unit cell containing one Li ion. The brown atoms residing in brown polyhedra are Fe^{2+} and the green atoms residing in green polyhedra are Fe^{3+}. (b) $LiFeBO_3$ unit cell containing one Li hole. (c) Structure of the most stable configuration of $Li_{0.5}FeBO_3$ with the unit cell indicated by the black box. The brown atoms residing in brown polyhedra are Fe^{2+} on which hole polarons can hop between, and the green atoms residing in green polyhedra are Fe^{3+} on which the electron polarons can hop between (polaronic transport is investigated in Sec. 3.7). The polaron-hopping paths A_e-B_e-C_e-D_e-A'_e and A_h-B_h-C_h-D_h-A'_h constitute the paths with the lowest barriers required to move electrons and holes, respectively, in the *c*-direction, where A_e, B_e, C_e, D_e, and A'_e denote Fe^{3+} sites and A_h, B_h, C_h, D_h, and A'_h denote Fe^{2+} sites. The positions of the Li ions in this configuration are given in Table S1 in Supporting Information. (d) Unit cell of half-lithiated phase with the Li-ion

configuration of the lowest-energy configuration, but with the Fe^{2+}–Fe^{3+} distribution predicted by the Coulombic model mentioned in the main text. (Images generated with the VESTA software package[19].)

All intermediate points in the range $0.0 < x < 0.5$ reside above the convex hull in Figure 2(a), suggesting that a two-phase reaction could occur in this region, possibly forming a stable $Li_{0.5}FeBO_3$–$FeBO_3$ interface during low-C-rate operation in which each phase has had sufficient time to reach its most stable Li configuration. However, this is not the case for the range $0.5 < x < 1.0$, where the lowest-energy configuration at $x = 0.75$ resides 3.3 meV/f.u. below a line connecting the lowest-energy configurations of the $Li_{0.5}FeBO_3$ phase and the $LiFeBO_3$ phase. This value is well below the typical accuracy of a DFT calculation, and it is therefore not possible to state with absolute certainty that the lowest-energy point at $x = 0.75$ lies below a line connecting the lowest-energy phases at $x = 0.5$ and $x = 1.0$, i.e., that the $Li_{0.75}FeBO_3$ phase is in fact stable. Additionally, even if the $Li_{0.75}FeBO_3$ phase was stable, kinetic effects during electrode operation might prevent this phase from reaching its lowest-energy configuration. This scenario would correspond to the formation of a stable interface between $Li_{0.5}FeBO_3$ and $LiFeBO_3$ during low-C-rate operation. Experiments performed at C/20 by Yamada et al.[2] and at C/30 and C/50 by Bo et al.[15,16] show that a two-phase reaction occurs between the half-lithiated phase and the fully lithiated phase (i.e., for $0.5 < x < 1.0$), and our phase-stability analysis indicates that a two-phase region between $LiFeBO_3$ and $Li_{0.5}FeBO_3$ could indeed be facilely formed and a further analysis of the role of the $Li_{0.5}FeBO_3$ phase is therefore undertaken.

3.3 Ionic transport in modulated $LiFeBO_3$ and $FeBO_3$. In order to determine the influence of the stable half-lithiated phase on the transport properties, NEB calculations were first performed on the modulated, lithiated phase, yielding activation barriers for a Li-hole jump in modulated $LiFeBO_3$, and on the fully delithiated phase, yielding activation barriers for Li-ions jumps in $FeBO_3$; the resulting activation barriers are shown in Figure 4. For transport along the *a*-axis, the motion of Li ions and Li holes occurs by a jump of 2.49 Å—henceforth referred to as A (following the jump notation of Seo et al.[8])—with an activation barrier of 0.29 and 0.40 eV for the Li ion and hole, respectively, followed by a 4.06 Å jump out of the LiO_4 chain—henceforth referred to as C—with an activation barrier of 1.85 eV for the Li ion. The same jump for a Li hole has a barrier of 1.74 eV, however, it is easier for the Li hole at site X in Figure 4(b) to move in the *a*-direction by performing D jumps (instead of C jumps) with a barrier of only 1.16 eV. The C (D) jump mechanism also constitutes the lowest-energy pathway in which the Li ions (holes) can jump in order to move between the corner-sharing LiO_4 chains shown in Figure 4(b). For Li transport along the *b*-axis, Li ions/holes are required to make a 5 Å jump, which would result in a prohibitively high activation barrier, effectively making this transport mechanism inactive. For ionic transport along the *c*-axis, the Li ions and holes have to overcome two barriers: An A jump (2.49 Å for Li ions and 3.10 Å for Li holes) with an activation barrier of 0.29 eV for the Li ions and 0.40 eV for the Li holes, and a jump of 3.58 Å for Li ions and 3.00 Å for Li holes—henceforth referred to as B (following the jump notation of Seo et al.[8])—with an activation barrier of 0.75 eV for Li ions and 0.61 eV for the Li holes. It is interesting to note, that Li at site X changes position from tetrahedron T_1 (vide Figure 4(b)) to T_2 (vide Figure 4(a)) upon full delithiation, at the same time

increasing the B jump length and decreasing the A jump length. This is also reflected in the activation barriers for Li-ion diffusion as the B barrier is more than twice the magnitude of the A barrier. The paths with their corresponding activation-barrier profiles are shown in Figure 4 and jump lengths, activation barriers and diffusivities are listed in Table 1. Additionally, we have calculated activation barriers for Li-hole diffusion in the unmodulated phase shown in Figure S1. However, the barriers do not change significantly compared to the modulated phase of $LiFeBO_3$.

a) Li-ion diffusion

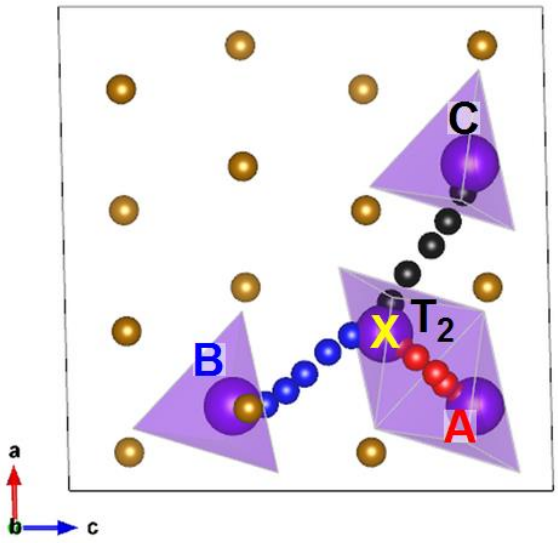

b) Li-hole diffusion

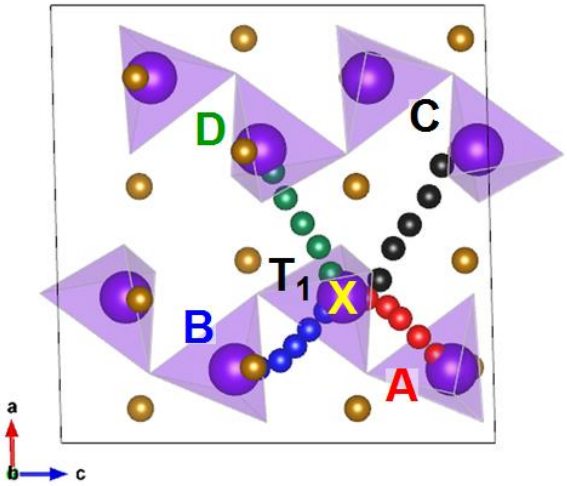

c)

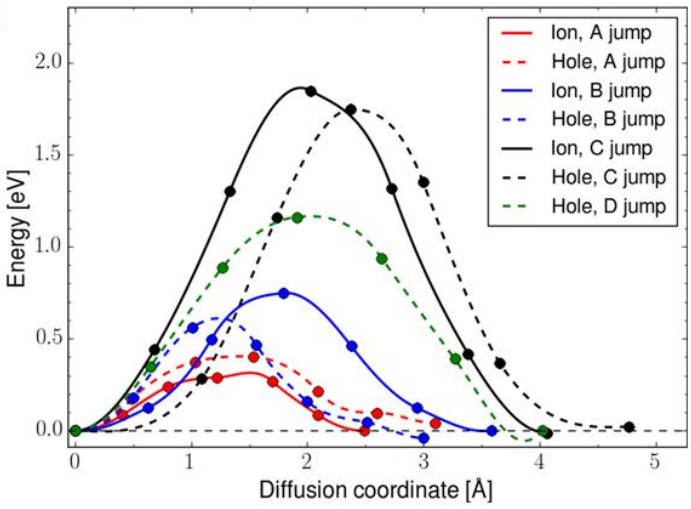

Figure 4. (a) Investigated Li-ion and Li-hole jumps in $FeBO_3$, (b) modulated $LiFeBO_3$ and (c) corresponding activation barriers. The most probable jumps for the Li ions and Li holes in the LiO_4 chains are A and B. Purple atoms are Li residing in purple polyhedra and brown atoms are Fe. The calculations were performed in a (2*a*,*b*,*c*) supercell. (Image in (a) generated with the VESTA software package[19].)

		Jump length, l [Å]	Activation barrier, E_{act} [eV]	DFT-calculated room-temperature diffusivity, D [cm^2/s]	Experimental diffusivity [cm^2/s]
Li ion in $FeBO_3$	A	2.49	0.29	$5.6 \cdot 10^{-15}$	$5.63 \cdot 10^{-14}$ [a]
	B	3.58	0.75		
	C	4.06	1.85		
Li hole in modulated $LiFeBO_3$	A	3.10	0.40	$1.3 \cdot 10^{-12}$	
	B	3.00	0.61		
	C	4.77	1.74		
	D	4.02	1.16		

Table 1. Jump lengths, activation barriers and the corresponding one-dimensional diffusional constants for Li transport in the *c*-direction. The channular diffusivity is calculated as $D = l^2k$, where l is the jump length and k is the total rate constant which is calculated from $k_{\mathrm{tot}}^{-1} = \sum_{n=1}^{N} k_n^{-1}\sigma_n$, where N is the number of jumps a Li ion/hole needs to perform in order to move in the *c*-direction, i.e., $N = 2$ (A or B), $k_n = \nu e^{-\frac{E_{\mathrm{act},n}}{k_B T}}$ is the rate constant for an elementary jump (i.e., A or B), where $\nu = 10^{13}$ s^{-1} is a typical prefactor, $E_{act,n}$ is the activation barrier for the n^{th} elementary jump, k_B is Boltzmann's constant and T is the absolute temperature, which is here taken to be room temperature, and σ_n is a symmetry factor, which in the present case is unity. [a] Diffusivity is for Li concentration below 0.5 (private communication with Cambaz et al.[31]).

A previous study by Seo et al.[8] found lower Li-hole barriers of 0.223 eV for the A jump and 0.437 eV for the B jump which correspond to a Li-hole diffusivity of about $3.7 \cdot 10^{-10}$ cm^2/s (here using a prefactor of $\nu = 10^{-13}$ s^{-1}). The apparent discrepancy between these barriers and our barriers most likely originates from the way the strongly correlated 3*d* electrons of Fe are described within the model. Seo et al.[8] applied a standard GGA approach, which is known to lack the correct description of the strongly localized *d* orbitals. To improve upon the description of the strongly localized orbitals of the Fe atoms, higher-level methods such as the *+U* correction (applied here) or hybrid functionals are often employed. However, it should be noted, that a *+U* correction will tend to penalize the movement of the diffusing species at the transition state of the migration process and thereby result in a possible overestimation of the activation barrier. Whereas the DFT barriers of Seo et al.[8] might be taken as a lower bound of the true activation barriers, the DFT+*U* -calculated barriers presented in this study serve as an upper bound on the true activation barriers. However, we point out that our calculated Li-ion diffusion coefficient of $5.6 \cdot 10^{-15}$ cm^2/s agrees well with the experimental value of $5.63 \cdot 10^{-14}$ cm^2/s measured by Cambaz et al.[31] using cyclic voltammetry, motivating our use of the Hubbard-*U*

correction. Despite the aforementioned barrier discrepancy, the ordering of the barriers, i.e., $E_b^A < E_b^B$, are consistent with the results of Seo et al.[8] even with the commensurate modulation included.

The calculations above—summarized in Table 1—show that the transport of Li ions and holes in bulk Li_xFeBO_3 occurs predominantly along the *c*-axis in nonlinear channels, constituted by corner-sharing LiO_4 complexes. Only two distinct types of jumps are needed for macroscopic transport, and the A and B jumps will thus dominate the macroscopic diffusion.

3.4 Ionic transport in $Li_{0.5}FeBO_3$. In order to obtain the kinetic barriers for Li diffusion in the half-lithiated phase, the energy of a Li configuration in which the Li-ion motion is constrained to one channel (extending along the *c*-axis) relative to the lowest-energy half-lithiated configuration was mapped out in Figure 5 (indicated by the blue line). In these channels, two Li ions, Li^1 and Li^2, move via the combined A and B jumps shown in Figure 4: The Li^2 jump between configuration A and B1 corresponds to an A jump in the endmembers ($FeBO_3$/$LiFeBO_3$), the Li^1 jump from configuration B1 to C corresponds to an endmember B jump, the Li^2 jump from configuration C to D1 corresponds to an endmember B jump, the Li^1 jump from configuration D1 to E corresponds to an endmember A jump, the Li^2 jump from configuration E to B2 corresponds to an endmember A jump, the Li^1 jump from configuration B2 to F corresponds to an endmember B jump, the Li^2 jump from configuration F to D2 corresponds to an endmember B jump and the Li^1 jump from configuration D2 to A corresponds to an endmember A jump. The smallest Li–Li distance in the channel is 3.40 Å in configuration A, 5.07 Å in configurations B1, B2, D1 and D2, 3.69 Å in configuration E and 2.98 Å in configurations C and F. NEB calculations were conducted on jumps between neighboring configurations and the activation barriers and Li-ion trajectories are shown in Figure S2 in Supporting Information. The activation barriers with the resulting jump rates are listed above each barrier in Figure 5. The barriers $E_2^{\rightarrow}$ and $E_7^{\leftarrow}$ both of 0.79 eV are slightly higher than the Li-ion barrier in $FeBO_3$ (0.75 eV) since the diffusing Li ion in each case approaches another Li ion in the channel (until Li–Li distance of 2.98 Å) and thereby increases its Coulombic repulsion. The diffusivity associated with two Li ions jumping from A to A (i.e., with a jump length of c = 10.35 Å) is $3.3 \cdot 10^{-26}$ cm^2/s, which is much lower than the diffusivity for both Li-ion in $FeBO_3$ ($5.6 \cdot 10^{-15}$ cm^2/s) and hole in $LiFeBO_3$ ($1.9 \cdot 10^{-12}$ cm^2/s) transport, indicating that the Li diffusion is strongly impeded in the half-lithiated phase.

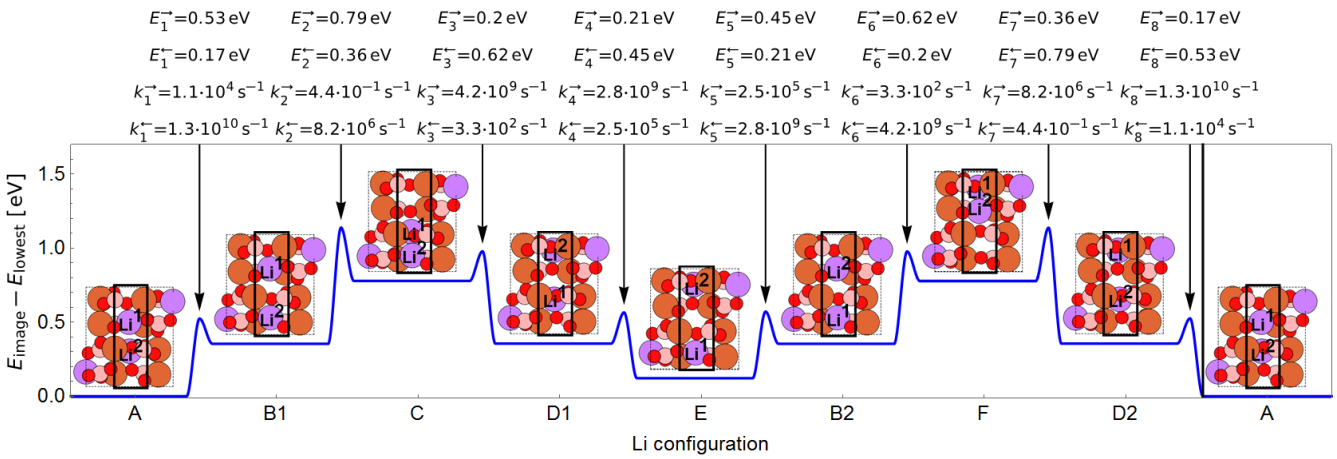

Figure 5. Energy landscape of two Li ions, Li^1 and Li^2, diffusing in the channel indicated by the thick black box in $Li_{0.5}FeBO_3$ simulated in the unit cell shown by the large black box. The kinetic barrier at $E_{\{1,\ldots,8\}}$ is the maximum barrier of the Li-ion jumps depicted in Figure S2 in Supporting Information, and the associated jump rate, $k_{\{1,\ldots,8\}}$, is also listed. B1 and B2 have identical Li distributions as do D1 and D2. The vertical line after D2 indicates the end of a full cycle (from A to D2). The coloring of the atoms follows that of Figure 1.

3.5 The $LiFeBO_3$–$Li_{0.5}FeBO_3$ interface. Our convex-hull analysis in Figure 2 and previous GITT experiments[2,15,16] suggest that a stable interface between a fully lithiated and half-lithiated phase could be formed. During discharge, Li ions from the $Li_{0.5}FeBO_3$ phase will accumulate at the interface between $LiFeBO_3$ and $Li_{0.5}FeBO_3$, and in order to determine the effects on the Li transport at this interface, the Li diffusion occurring in close vicinity of an interface between $LiFeBO_3$ containing a Li hole and $Li_{0.5}FeBO_3$ was investigated through a NEB calculation. The pathway with the associated activation barrier is shown in Figure 6. Also indicated is the energy level of the interface structure in which the Li hole resides at the interface in the Li-poor region ($Li_{0.5}FeBO_3$) which is about 0.1 eV higher than having the Li hole in the Li-rich region (green point). The barriers during charge (0.32 eV) and discharge (0.19 eV) are both much lower compared to the diffusion barriers of Li ions in $FeBO_3$ and Li holes in $LiFeBO_3$. This is not surprisingly, since Li diffusion across the $LiFeBO_3$–$FeBO_3$ interface—found in Fig S3 in Supporting Information—also displayed lower barriers than those for Li-ion/hole in $FeBO_3$/$LiFeBO_3$. Hence, Li diffusion in the interfacial region between the $LiFeBO_3$ phase containing a Li hole and the $Li_{0.5}FeBO_3$ phase is not expected to be impeded due to the interfaces per se.

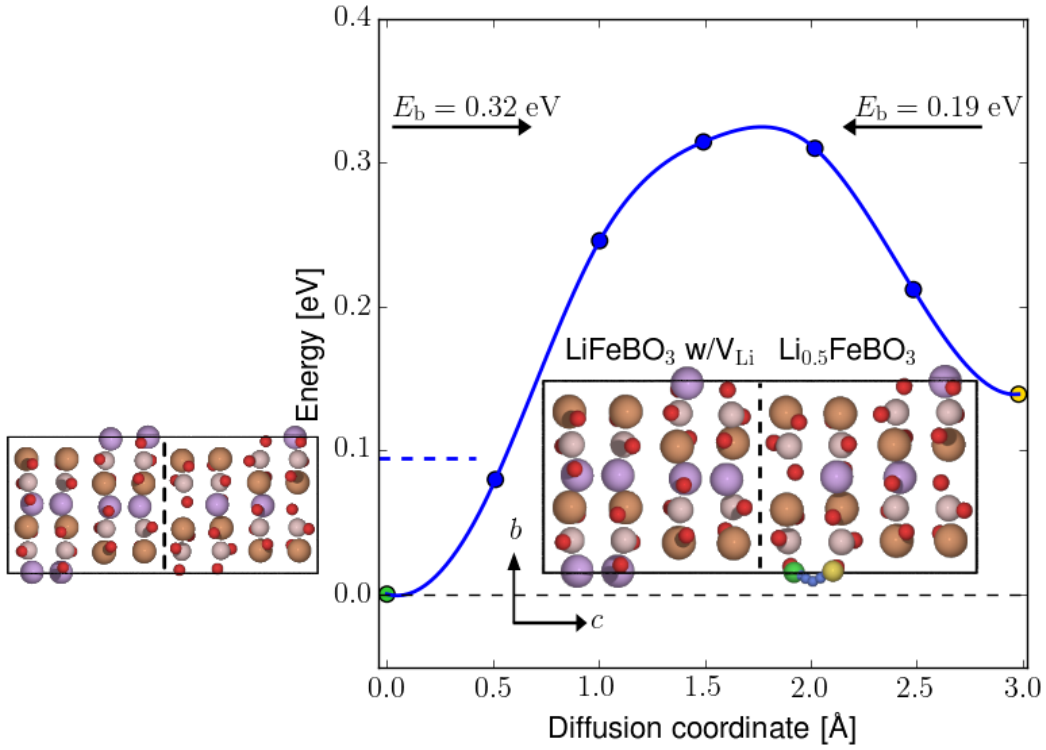

Figure 6. Activation-barrier profile for lithium diffusion in the half-lithiated phase (right part of the big inset structure) near the phase boundary between $LiFeBO_3$ containing a Li hole and $Li_{0.5}FeBO_3$ indicated by the vertical dashed line in the right inset. The diffusing Li ion is indicated by green (initial position), blue (intermediate positions) and yellow (final position). The energy of the interface containing the Li hole in the half-lithiated region (left inset) is indicated by the blue dashed line at 0.1 eV. The coloring of the rest of the atoms follows that of Figure 1. As our previous NEB calculations revealed (vide Sec. 3.3), the Li-hole transport is essentially unaffected by the modulation effects, and the calculations here were therefore performed in a (*a*,*b*,2*c*) supercell of unmodulated $LiFeBO_3$ and $Li_{0.5}FeBO_3$.

3.6 Electronic transport. During discharge of the $Li_{0.5}FeBO_3$ phase, hole polarons have to traverse a shell of the $LiFeBO_3$ phase in order to recombine with Li ions being inserted into the $Li_{0.5}FeBO_3$ core. In the following, investigations of electron-polaron transport in $FeBO_3$ and hole-polaron transport in $LiFeBO_3$ have been conducted to determine possible polaronic limitations to the charge–discharge process.

We found that upon adding (removing) an electron to $FeBO_3$ (from modulated $LiFeBO_3$), an electron (hole) polaron was localized at an Fe^{3+} (Fe^{2+}) ion, increasing (decreasing) the bond lengths by 0.14 Å (0.12 Å) and changing the magnetic moment from 4.29 μ_B (3.75 μ_B) to 3.79 μ_B (4.27 μ_B). According to the Mulliken criterion[32] calculated magnetic moments of 3.75 μ_B and 3.79 μ_B correspond to a nominal magnetic moment of 4 μ_B originating from the unpaired spin counts of the d^6 ion Fe^{2+}, and 4.29 μ_B and 4.27 μ_B correspond to a nominal magnetic moment of 5 μ_B originating from the unpaired

spin counts of the d^5 ion Fe^{3+}. In the lowest-energy configuration of the half-lithiated phase shown in Figure 3, an electron (hole) polaron was found to be more stable than a delocalized electron (hole) by 0.65 eV (0.47 eV). In $Li_{0.5}FeBO_3$, the polaron-hosting Fe ion showed the same trends as those in the active endmembers: Upon adding (removing) an electron to $Li_{0.5}FeBO_3$ (from modulated $LiFeBO_3$), an electron (hole) polaron was localized at a neighboring Fe^{3+} (Fe^{2+}) ion, an increase (decrease) in the Fe–O bond lengths by 0.13 Å (0.12 Å) and a moment change from 4.27 μ_B (3.77 μ_B) to 3.76 μ_B (4.29 μ_B)—corresponding to nominal magnetic moment 4 μ_B (5 μ_B)—was observed, proving the existence of electron and hole polarons in the half-lithiated phase.

In order to determine possible limitations on the electrochemical performance of Li_xFeBO_3 originating from effects related to the electronic transport, NEB calculations of polaron jumps in bulk $FeBO_3$ and $LiFeBO_3$ were conducted for feasible electron- and hole-polaron hops—shown in Figure 7—namely polaron hop from Fe site A_p to Fe site B_p (abbreviated A_p-B_p), polaron hop from Fe site A_p to Fe site C_p (abbreviated A_p-C_p), polaron hop from Fe site Ap to Fe site D_p (abbreviated A_p-D_p), polaron hop from Fe site A_p to Fe site E_p (abbreviated A_p-E_p), polaron hop from Fe site A_p to Fe site F_p (abbreviated A_p-F_p), polaron hop from Fe site A_p to Fe site G_p (abbreviated A_p-G_p) and polaron hop from Fe site A_p to Fe site H_p (abbreviated A_p-H_p) with the associated calculated NEB barriers shown in Figure 7 (b) and (c). Movement of both electron and hole polarons along the *a*-axis as well as along the *b*-axis is possible via two A_p-D_p hops with the barrier being 0.15 eV for the hole polaron and 0.14 eV for the electron polaron. The movement of polarons along the *c*-axis is achieved by the combined hopping mechanism of A_p-B_p, A_p-C_p and A_p-H_p with the highest barrier being 0.15 eV (A_p-H_p hop) for the hole polaron and 0.19 eV (A_p-C_p hop) for the electron polaron. All electron-polaron activation barriers are seen to be well below the delocalization energy of 0.57 eV (vide Figure 7) required to delocalize the electron polaron. It was not possible to find a delocalized solution for hole polarons in the modulated phase indicating that hole polarons are particularly stable in this phase. Additionally, we have calculated the activation barriers for hole-polaron hopping in unmodulated $LiFeBO_3$ which are shown in Figure S4 in Supporting Information, and by comparing these results with those for the modulated phase in Figure 7(c), no significant change in the hole-polaron barriers upon modulation is observed.

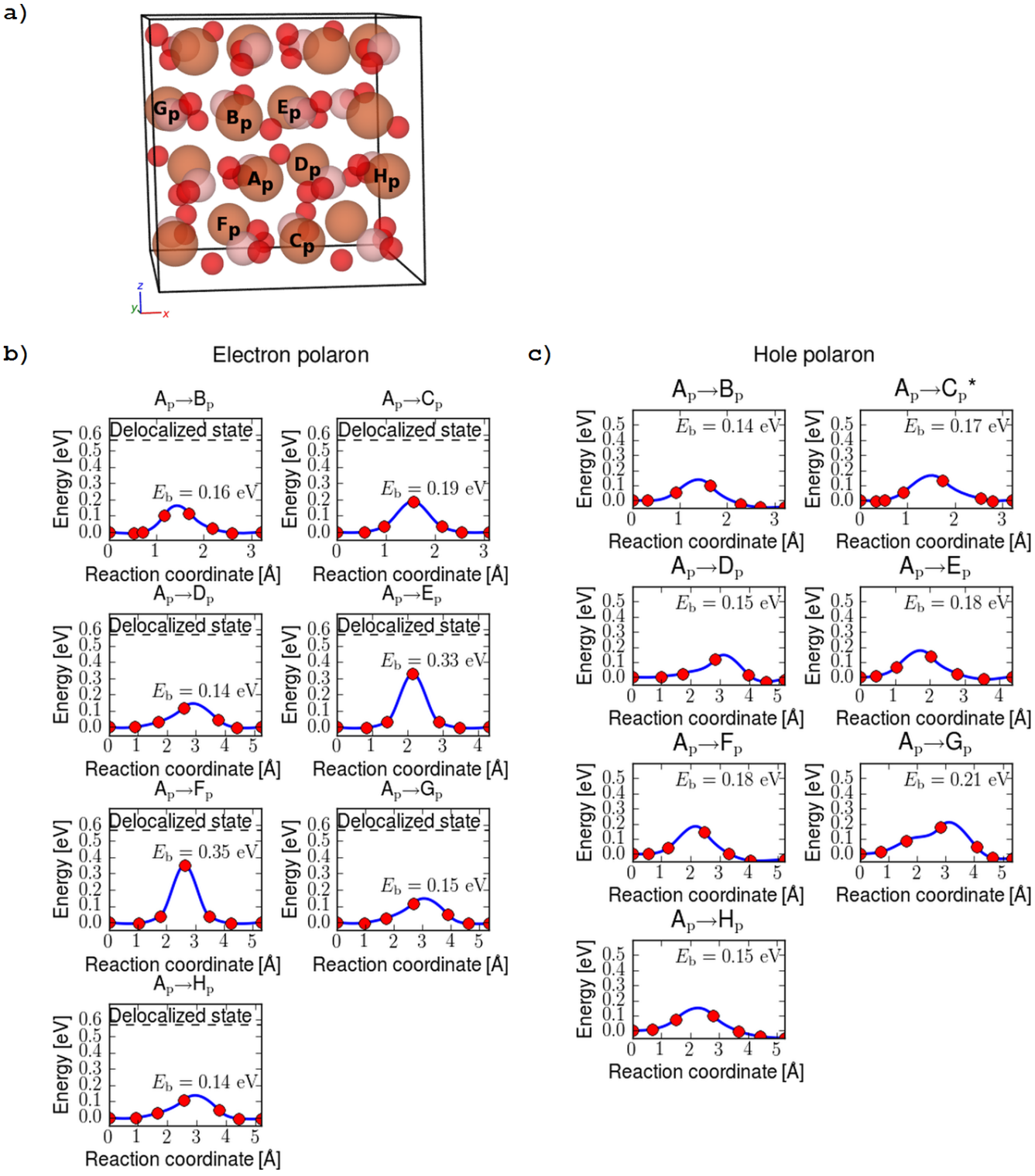

Figure 7. (a) Polaronic hops from Fe site A_p to neighboring Fe sites B_p, C_p, D_p, E_p, F_p, G_p and H_p with associated activation barriers for (b) electron-polaron hops in $FeBO_3$ and (c) hole-polaron hops in $LiFeBO_3$. * This hole-polaron hop between A_p and C_p is that of the unmodulated phase.

Considering the most stable half-lithiated structure in Figure 3 found in the convex-hull analysis of Figure 2, for a hole polaron hopping through this half-lithiated phase, the highest barrier for the lowest-barrier path, A_h-B_h-C_h-D_h-A'_h, is 0.21 eV (the B_h-C_h hop in Figure 3(c)). During charge, a hole polaron could still travel through the half-lithiated phase, but the barrier is increased to 0.21 eV from the 0.15 eV barrier in the fully delithiated phase (assuming that the polaron barrier of each individual hop does not change significantly upon changing the Li concentration). Likewise, for an electron polaron propagating in the half-lithiated phase, the highest barrier associated with the lowest-barrier path, A_e-B_e-C_e-D_e-A'_e, is 0.35 eV (the A_e-B_e hop in Figure 3(c)). During discharge, an electron polaron could still travel through the half-lithiated phase, but the barrier is increased to 0.35 eV from the 0.19 eV barrier in the fully delithiated phase. Hence, the electronic mobility during both charge and discharge is predicted to be lowered in the half-lithiated phase (vide Figure 3) compared to the pristine phases.

Bo et al.[16] experimentally observed an increase in the difference in charge and discharge potentials—giving rise to an overvoltage of more than 0.5 V at C/30—during charging of $LiFeBO_3$ to $Li_{0.5}FeBO_3$ (vide their Figure 1). This can be related to our model in the following way: During charge, a region of $Li_{0.5}FeBO_3$ will be formed around the $LiFeBO_3$ nanoparticle and due to the higher activation barriers for ionic and polaronic transport in $Li_{0.5}FeBO_3$ relative to $FeBO_3$ and $LiFeBO_3$, a higher electric field is required to drive the delithiation process, which manifests itself as an increase in the charge–discharge potential difference. During discharge of $Li_{0.5}FeBO_3$, a $LiFeBO_3$ phase would form around the $Li_{0.5}FeBO_3$ core, and since the barriers for Li diffusion in bulk $LiFeBO_3$ and across the $LiFeBO_3$–$Li_{0.5}FeBO_3$ interface are relatively low compared to those of Li diffusion in $Li_{0.5}FeBO_3$, no significant charge–discharge difference related to Li diffusion is expected to occur. This is supported by the charge–discharge data in Figure 1 in Bo et al.[16] as the charge–discharge potential difference is observed to decrease during discharge.

The intrinsically poor conduction of both Li ions and electron/hole polarons in the most stable intermediate phase, $Li_{0.5}FeBO_3$, might not be restricted to $LiFeBO_3$, but could also exist in other lithiated transition-metal borate, such as those containing Mn and Co as these are also suggested to have their lithium diffusion kinetically limited.[33] The phase-stability analysis and path techniques employed in the present work could be used to explain whether these Li-electrode materials suffer from the same fundamental limitations as the $LiFeBO_3$ electrode. Besides down-sizing the $LiFeBO_3$ nanoparticles to decrease the diffusion path length, recent studies[34,35] have shown that substitution of Fe by other transition metals could improve the poor transport properties of $LiFeBO_3$.

4. CONCLUSIONS

In this work, the structural and kinetic properties of Li_xFeBO_3 were investigated using Hubbard-corrected density functional theory, including the effects from the previously reported commensurate structural modulation of $LiFeBO_3$. A thermodynamic phase-stability analysis revealed a particularly stable half-lithiated phase together with a relatively stable $Li_{0.75}FeBO_3$ phase, whereas the $Li_{0.875}FeBO_3$ phase predicted to be stable by Yamada et al.[2] was not found to be stable in our study. Our barriers for Li-ion and hole transport in bulk Li_xFeBO_3 phases indicated highly anisotropic Li-ion motion with the lowest-barrier pathway being along the *c*-axis with associated diffusivities of $5.6 \cdot 10^{-15}$ cm^2/s for Li-ion diffusion in good agreement with experiments ($5.6 \cdot 10^{-14}$ cm^2/s). It was shown that the Li diffusion in the bulk of $Li_{0.5}FeBO_3$ limited the overall Li diffusion in the active material. Electronic conduction was shown to be mediated by small electron and hole polarons with relatively low hopping barriers in $FeBO_3$ and $LiFeBO_3$, but relatively high hopping barriers in $Li_{0.5}FeBO_3$. This barrier increase lowers the mobility of the polarons as they enter the half-lithiated phase. On the contrary, the Li diffusion in the vicinity of an interface between $LiFeBO_3$ containing a hole and $Li_{0.5}FeBO_3$ during charge/discharge is not expected to reduce the overall Li-ion/hole diffusion in Li_xFeBO_3, since the associated kinetic barriers are lower than those associated with Li-ion/hole diffusion in the delithiated/lithiated phases. Interestingly, the barriers for Li-hole diffusion and hole-polaron hopping in the modulated phase were found to the same as those for the unmodulated phase. Hence, in the transport model presented here, the combined intrinsic reduction of Li-ion and electron/hole polaron mobility in bulk $Li_{0.5}FeBO_3$ relative to $LiFeBO_3$ and $FeBO_3$ could explain the experimentally reported large overvoltage at initial-stage delithiation of $LiFeBO_3$. Remedies for these transport-related issues might be found in decreasing the size of the $LiFeBO_3$ particles and substituting some of the Fe atoms by other cations[34]. Work along this line is now underway.

ASSOCIATED CONTENT

Supporting Information

Fractional coordinates of the Li atoms in the most stable configuration of $Li_{0.5}FeBO_3$, NEB-calculated activation barriers for Li-hole diffusion in unmodulated $LiFeBO_3$, NEB-calculated activation barriers for diffusion of Li ions in half-lithiated phases, results on calculations of transport across the $LiFeBO_3$–$FeBO_3$ interface and NEB-calculated activation barriers for hole-polaron hopping in unmodulated $LiFeBO_3$.

AUTHOR INFORMATION

Corresponding Author

*E-mail: teve@dtu.dk. Tel: +45 51641787

Notes
The authors declare no competing financial interest.

ACKNOWLEDGEMENTS

The research leading to these results has received funding from the European Union's Seventh Framework Programme (FP7/2007-2013) under grant agreement n° 608575. JMGL acknowledges support from the Spanish Ministry of Economy and Competitiveness under Projects FIS2012-30996 and FIS2013-46159-C3-1-P and from the Villum Foundation's Young Investigator Programme (4th round, project: *In silico design of efficient materials for next generation batteries.* Grant number: 10096).

REFERENCES

(1) Yabuuchi, N.; Ohzuku, T. Novel Lithium Insertion Material of $LiCo_{1/3}Ni_{1/3}Mn_{1/3}O_2$ for Advanced Lithium-Ion Batteries. *J. Power Sources* **2003**, *119-121*, 171–174.

(2) Yamada, A.; Iwane, N.; Harada, Y.; Nishimura, S.; Koyama, Y.; Tanaka, I. Lithium Iron Borates as High-Capacity Battery Electrodes. *Adv. Mater.* **2010**, *22* (32), 3583–3587.

(3) Park, M.; Zhang, X.; Chung, M.; Less, G. B.; Sastry, A. M. A Review of Conduction Phenomena in Li-Ion Batteries. *J. Power Sources* **2010**, *195* (24), 7904–7929.

(4) Hohenberg, P.; W. Kohn. Inhomogeneous Electron Gas. *Phys. Rev.* **1964**, *136* (3B), B864–B871.

(5) Kohn, W.; Sham, L. J. Self-Consistent Equations Including Exchange and Correlation Effects. **1965**, *140* (4A), A1133–A1138.

(6) Ceder, G.; Persson, K. How Supercomputers Will Yield a Golden Age of Materials Science. *Scientific American*. 2013, pp 34–40.

(7) Morgan, D.; Van der Ven, A.; Ceder, G. Li Conductivity in Li_xMPO_4 (M=Mn , Fe , Co , Ni) Olivine Materials. *Electrochem. Solid-State Lett.* **2004**, *7* (2), A30–A32.

(8) Seo, D.-H.; Park, Y.-U.; Kim, S.-W.; Park, I.; Shakoor, R.; Kang, K. First-Principles Study on Lithium Metal Borate Cathodes for Lithium Rechargeable Batteries. *Phys. Rev. B* **2011**, *83* (20), 205127:1–8.

(9) Ong, S. P.; Chevrier, V. L.; Ceder, G. Comparison of Small Polaron Migration and Phase Separation in Olivine $LiMnPO_4$ and $LiFePO_4$ Using Hybrid Density Functional Theory. *Phys. Rev. B* **2011**, *83* (7), 0751121–0751127.

(10) Ong, S. P.; Mo, Y.; Ceder, G. Low Hole Polaron Migration Barrier in Lithium Peroxide. *Phys.*

Rev. B **2012**, *85* (8), 2–5.

(11) Garcia-Lastra, J. M.; Myrdal, J. S. G.; Christensen, R.; Thygesen, K. S.; Vegge, T. DFT+*U* Study of Polaronic Conduction in Li_2O_2 and Li_2CO_3: Implications for Li–air Batteries. *J. Phys. Chem. C* **2013**, *117* (11), 5568–5577.

(12) Mekonnen, Y. S.; Garcia-Lastra, J. M.; Hummelshøj, J. S.; Jin, C.; Vegge, T. Role of Li_2O_2@Li_2CO_3 Interfaces on Charge Transport in Nonaqueous Li–Air Batteries. *J. Phys. Chem. C* **2015**, *119* (32), 18066–18073.

(13) Sharma, N.; Guo, X.; Du, G.; Guo, Z.; Wang, J.; Wang, Z.; Peterson, V. K. Direct Evidence of Concurrent Solid-Solution and Two-Phase Reactions and the Nonequilibrium Structural Evolution of $LiFePO_4$. *J. Am. Chem. Soc.* **2012**, *134* (18), 7867–7873.

(14) Ouyang, C.; Shi, S.; Wang, Z.; Huang, X.; Chen, L. First-Principles Study of Li Ion Diffusion in $LiFePO_4$. *Phys. Rev. B* **2004**, *69* (10), 104303.

(15) Bo, S.-H.; Wang, F.; Janssen, Y.; Zeng, D.; Nam, K.-W.; Xu, W.; Du, L.-S.; Graetz, J.; Yang, X.-Q.; Zhu, Y.; Parise, J. B.; Grey, C. P.; Khalifah, P. G. Degradation and (De)lithiation Processes in the High Capacity Battery Material $LiFeBO_3$. *J. Mater. Chem.* **2012**, *22* (18), 8799–8809.

(16) Bo, S. H.; Nam, K. W.; Borkiewicz, O. J.; Hu, Y. Y.; Yang, X. Q.; Chupas, P. J.; Chapman, K. W.; Wu, L.; Zhang, L.; Wang, F.; Grey, C. P.; Khalifah, P. G. Structures of Delithiated and Degraded $LiFeBO_3$, and Their Distinct Changes upon Electrochemical Cycling. *Inorg. Chem.* **2014**, *53* (13), 6585–6595.

(17) Legagneur, V.; An, Y.; Mosbah, A.; Portal, R.; Le Gal La Salle, A.; Verbaere, A.; Guyomard, D.; Piffard, Y. $LiMBO_3$ (M = Mn, Fe, Co): Synthesis, Crystal Structure and Lithium Deinsertion/insertion Properties. *Solid State Ionics* **2001**, *139* (1-2), 37–46.

(18) Janssen, Y.; Middlemiss, D. S.; Bo, S. H.; Grey, C. P.; Khalifah, P. G. Structural Modulation in the High Capacity Battery Cathode Material $LiFeBO_3$. *J. Am. Chem. Soc.* **2012**, *134* (30), 12516–12527.

(19) Momma, K.; Izumi, F. VESTA 3 for Three-Dimensional Visualization of Crystal, Volumetric and Morphology Data. *J. Appl. Crystallogr.* **2011**, *44* (6), 1272–1276.

(20) Bahn, S. R.; Jacobsen, K. W. An Object-Oriented Scripting Interface to a Legacy Electronic Structure Code. *Comput. Sci. Eng.* **2002**, *4* (3), 56–66.

(21) Kresse, G.; Furthmöller, J. Efficiency of Ab-Initio Total Energy Calculations for Metals and Semiconductors Using a Plane-Wave Basis Set. *Comput. Mater. Sci.* **1996**, *6* (1), 15–50.

(22) Blöchl, P. E. Projector Augmented-Wave Method. *Phys. Rev. B* **1994**, *50* (24), 17953–17979.

(23) Perdew, J. P.; Burke, K.; Ernzerhof, M. Generalized Gradient Approximation Made Simple. *Phys. Rev. Lett.* **1996**, *77* (18), 3865–3868.

(24) Blöchl, P. E.; Jepsen, O.; Andersen, O. K. Improved Tetrahedron Method for Brillouin-Zone Integrations. *Phys. Rev. B* **1994**, *49* (23), 16223–16233.

(25) Islam, M. S.; Fisher, C. A. J. Lithium and Sodium Battery Cathode Materials: Computational Insights into Voltage, Diffusion and Nanostructural Properties. *Chem. Soc. Rev.* **2014**, *43* (1), 185–204.

(26) Meng, Y. S.; Arroyo-de Dompablo, M. E. First Principles Computational Materials Design for Energy Storage Materials in Lithium Ion Batteries. *Energy Environ. Sci.* **2009**, *2* (6), 589.

(27) Anisimov, V. I.; Aryasetiawan, F.; Lichtenstein, I. First-Principles Calculations of the Electronic Structure and Spectra of Strongly Correlated Systems: The LDA+*U* Method. *J. Phys. Condens. Matter* **1997**, *9* (997), 767–808.

(28) Monkhorst, H. J.; Pack, J. D. Special Points for Brillouin-Zone Integrations. *Phys. Rev. B* **1976**, *13* (12), 5188–5192.

(29) Bitzek, E.; Koskinen, P.; Gähler, F.; Moseler, M.; Gumbsch, P. Structural Relaxation Made Simple. *Phys. Rev. Lett.* **2006**, *97* (17), 1–4.

(30) Jónsson, H.; Mills, G.; Jacobsen, K. W. Nudged Elastic Band Method for Finding Minimum Energy Paths of Transitions. *Class. Quantum Dyn. Condens. Phase Simulations - Proc. Int. Sch. Phys.* **1998**, 385–404.

(31) Cambaz, M. A.; Anji Reddy, M.; Vinayan, B. P.; Witte, R.; Pohl, A.; Mu, X.; Chakravadhanula, V. S. K.; Kübel, C.; Fichtner, M. Mechanical Milling Assisted Synthesis and Electrochemical Performance of High Capacity $LiFeBO_3$ for Lithium Batteries. *ACS Appl. Mater. Interfaces* **2016**, *8* (3), 2166–2172.

(32) Mulliken, R. S. Electronic Population Analysis on LCAO-MO Molecular Wave Functions. I. *J. Chem. Phys.* **1955**, *23* (10), 1833–1840.

(33) Masquelier, C.; Croguennec, L. Polyanionic (Phosphates, Silicates, Sulfates) Frameworks as Electrode Materials for Rechargeable Li (or Na) Batteries. *Chem. Rev.* **2013**, *113* (8), 6552–6591.

(34) Kim, J. C.; Seo, D.-H.; Ceder, G. Theoretical Capacity Achieved in a $LiMn_{0.5}Fe_{0.4}Mg_{0.1}BO_3$ Cathode by Using Topological Disorder. *Energy Environ. Sci.* **2015**, *8* (6), 1790–1798.

(35) Li, A.; Xu, L.; Li, C.; Qian, Y. Q. Mesh-like $LiZnBO_3$/C Composites as a Prominent Stable Anode for Lithium Ion Rechargeable Batteries. *J. Mater. Chem. A* **2016**, *4*, 5489–5494.